Full length article

Hardening under compression in Au foams

Carlos J. Ruestes [a, *], Diana Farkas [b], Alfredo Caro [c], Eduardo M. Bringa [a]

[a] CONICET and Facultad de Ciencias Exactas y Naturales, Universidad Nacional de Cuyo, Mendoza 5500, Argentina
[b] Department of Materials Science and Engineering, Virginia Polytechnic Institute and State University, Blacksburg, VA 24061, USA
[c] Materials Science and Technology Division, Los Alamos National Laboratory, Los Alamos, NM 87544, USA

ABSTRACT

We report the results of compressive tests for a model bi-continuous nanoporous gold structure using atomistic simulations focusing on the densification regime and the plasticity mechanisms taking place. The stress − strain response follows a logarithmic evolution proportional to the inverse of strain and we provide a simple scaling law for this behavior. Hardening is correlated to the dislocation density and an exponential dependence is revealed. The plasticity mechanisms were inspected revealing the presence of Hirth and Frank partials contributing to the hardening of the sample. Lomer−Cottrel locks, perfect dislocations, and twinning were also found.

© 2016 Acta Materialia Inc. Published by Elsevier Ltd. All rights reserved.

1. Introduction

Metallic foams with pore and ligament sizes in the nanoscale offer outstanding properties and an ever increasing range of applications. With respect to their mechanical properties, several studies had shown that the Gibson−Ashby equation for macroscale foams fails to predict the observed strengths [1−3], moreover, a recent contribution by Farkas et al. [2] has shown a substantial tension/compression asymmetry for nanometer-sized ligament foams and even the densification of Au foams under tension. Regarding their application, their high surface-to-volume ratio makes them ideal candidates for catalysis applications [4−6], and had opened the door to surface-chemistry-powered actuators and sensors [7−13]. The potential for applications extend to lightweight structural panels, heat sinks, energy absorption devices to name a few [14]. These characteristics together with the possibility of ligaments reaching theoretical strength limits attract much attention to these materials. Due to its ease of fabrication and novel properties, nanoporous gold (np-Au) is a model system for the study of the mechanical properties and plasticity mechanisms at the nanoscale.

Significant efforts have been devoted to study the mechanical properties of np-Au [15−17], its yield strength and elastic modulus have been experimentally measured using nanoindentation [17] and microtension [18]. In the absence of a specific model for nanoscale porosity, the Gibson−Ashby model [19] has been extensively used for theoretical studies of nanoporous foams to estimate their elastic modulus, yield strength and ultimate tensile strength based solely on the relative mass density and a few constants. With a remarkable success in matching the performance of micron-scale porous materials, the standard Gibson−Ashby scaling relation is not applicable to nanoporous gold since the derived yields strengths do not agree with experimental values and the nanoporous metal yield strength varies as a function of ligament diameter [1], this has been recently revisited by Briot and Balk [3]. Fruitful contributions presented modified scaling laws for nanoporous foams [1,3,20−22]. While significant efforts have been directed to study the strain hardening of ALPORAS foams [23], less is known with respect to Au foams strain hardening, particularly at the nanoscale.

The objective of this paper is to shed light into the deformation mechanisms, mechanical properties and scaling laws for the late part of the plastic yielding plateau and the densification stage of nanoporous foams deformation. We present an atomistic study of the mechanical response of Au nanofoams under compression. Deformation leads to defects, including stacking faults (SF), twins, and dislocations. By averaging atomic quantities we produce plots of typically used macroscale quantities and derive scaling laws for the plastic yielding plateau stage and the densification stage.

---

* Corresponding author.
E-mail address: cjruestes@hotmail.com (C.J. Ruestes).

2. Methods

Our simulations were performed using the MD computer code LAMMPS [24] with an embedded atom model potential (EAM) to describe Au properties [25]. The nanofoam was created using a phase-field model emulating the spinodal decomposition of a Au–Ag mixture, where the Ag component is then removed to generate the foam, using periodic boundary conditions in all three directions, as described in Refs. [22,26,27]. The sample dimensions were $21 \times 21 \times 107$ nm^3 with the loading axis aligned to the z-axis. The resulting foam had an average ligament diameter of 1.8 nm and a pore fraction of 75%. The sample lateral dimensions x and y were almost 12 times the average ligament diameter, resulting in a cross-section including enough filaments to ensure that box size does not play a role in the mechanical response of the foam. Samples with different aspect ratios were also tested, without significant differences. A Nose-Hoover thermostat and barostat was used. The structures were equilibrated at 1 K for 500 ps. After equilibration, and in an attempt to mimic strain-controlled compressive mechanical deformation tests, the sample was uniaxially compressed along the [001]-direction by re-scaling its longest dimension at a strain rate of 3×10^8 s^{-1} while temperature was maintained constant at 1 K. Defect tracking and identification was performed by means of the Crystal Analysis Tool [28]. This code is capable of identifying a wide variety of linear and planar defects. Atomistic visualization was performed by means of OVITO [29] and ParaView [30].

3. Results and discussion

3.1. Mechanical response

The evolution of the sample porosity was computed by means of a built-in surface geometry reconstruction algorithm in OVITO [29] that allows for the computation of void surfaces and volume. In short, it implements the so-called "rolling ball" method, yielding the surface area accessible to a probe sphere. Only space regions that are accessible to the probe are considered empty, and solid otherwise. The details of the algorithm can be found in Ref. [31]. Fig. 1 presents the evolution of the sample porosity together with snapshots of a slice of the sample at the beginning and ending of the simulation. Porosity reduction begins with an almost linear stage corresponding to the early stages of plasticity up to 0.2–0.3 strain. Slightly after the strain reaches 0.3 the densification stage begins (see Fig. 2) and the slope of porosity reduction increases as pore collapsing proceeds. Fig. 2 shows the stress–strain curve
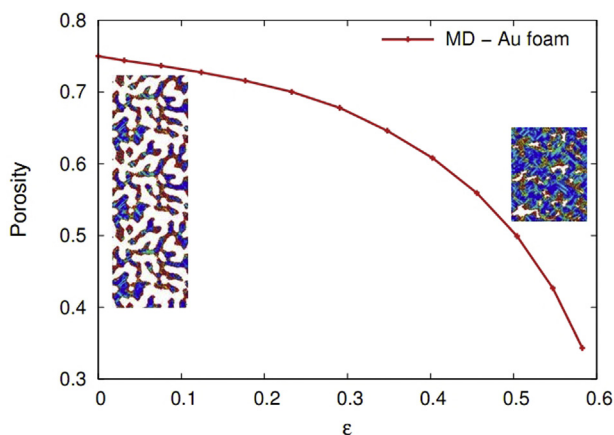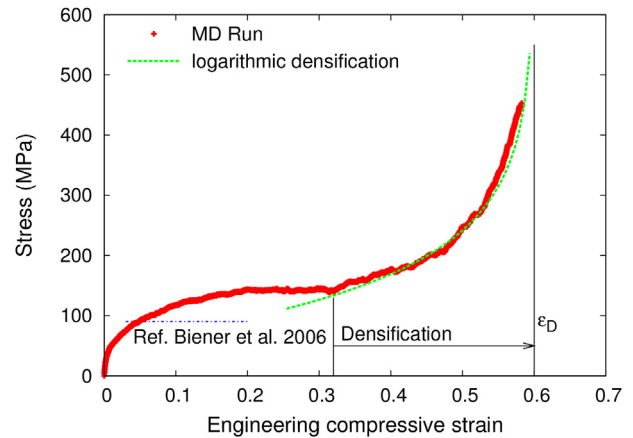
Fig. 2. Stress–strain curve for our simulations. Horizontal blue line indicates the plateau by Biener et al. [17]. Green curve indicates our proposed densification model. Densification process initiates at a strain of 0.32 and stress increases asymptotically as the strain reaches the full densification strain. (For interpretation of the references to colour in this figure legend, the reader is referred to the web version of this article.)

obtained during the compression of the sample. The curve essentially presents three stages, an almost linear elastic regime, followed by a plastic yielding regime and finally a densification regime. The deformation is elastic for strains up to 0.01 with an elastic modulus of 3.5 GPa, in agreement with Farkas et al. [2] and similar to the results of Sun and co-workers [22]. Experimentally, Biener et al. [17] obtained elastic modulus of the order of 2 GPa when studying nanoporous gold micropillars of 4 micron diameter and 40 nm ligament size under microcompression testing. Dou and Derby [32] reached an elastic modulus of around 1 GPa when testing nanoporous gold nanowires. Visual inspection of Fig. 2 shows that a strain of 0.02 triggers plasticity and the yield strength was found to be 50 MPa, a value close to that found experimentally by Jin et al. [33] for a np Au sample with 15 nm ligament diameter under compression tests. The horizontal blue line in Fig. 2 represents the yield strength for uniaxial microcompression tests of a 4 micron diameter np-Au column with a relative density of 0.3 and a ligament diameter of 40 nm, as reported by Biener and co-workers [17]. The authors also report on 0.25 relative density np-Au nanoindentation experiments, which for samples with ligament size of 10 nm reach a hardness in the range of 136–206 MPa. By applying the simple, yet questionable at this scale, Tabor relationship (Hardness = 3 times the Yield Strength) to those values, the expected yield strength can be placed in the range of 45–69 MPa. The plateau on the stress strain curve for our simulations occurs roughly at a stress of 140 MPa, twice as much as the upper limit in the derived range and also higher than the plateau values experimentally by Jin et al. [33]. This is not unexpected due to the high strain-rates used in MD simulations in comparison to the quasi-static nature of experimental tests.

Our previous study [2] focused in the foam behavior below 0.3 deformation, where most foams show a stress plateau while the filaments are crushed. The plateau is assumed to end when the foam has compacted and a hardening behavior starts in the fully compacted phase [19]. Ashby's scaling laws might have to be modified at the nanoscale, including Hall–Petch type corrections [1,15] and corrections due to surface stress [34]. Jin et al. [33] had shown that the overall shape of stress–strain curves at large strains is also maintained for nanofoams. In order to test the mechanisms behind this behavior at the nanoscale, here we have extended our compression simulations [2] to reach almost 0.6 strain deformation. We do observe an end to the stress plateau and the beginning

Fig. 1. Evolution of the sample porosity with strain.

of a hardening regime, with the overall shape of the stress–strain curve reminiscent of the curves by Jin et al. [33]. At the end of the stress–strain plot, the hardening modulus approaches 3 GPa. While this value might appear excessively high, high strain rate compression effects would lead to an increase in hardening modulus compared to quasi-static experiments.

Fig. 3 presents a typical stress-relative density plot for our simulations, together with simple power law models. At small densities (small strains), a power law of 1/2 is expected, with a good performance in the range from 0.33 to 0.35, that is, at the early stages of plasticity.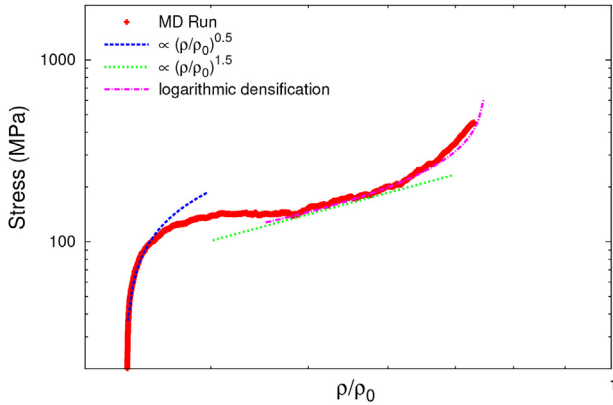 Then the stress curve shows a plateau up to a relative density of 0.5. Above 0.5 the stress falls into the first hardening stage following a 3/2 power law until a relative density of around 0.6 is reached. Above that density, a stronger hardening behavior is obtained. This suggests that a modification to the Hall–Petch relation seems necessary. At relatively low strain, surface stress can generate a strong tension/compression asymmetry and modify the typical Hall–Petch behavior [2]. The need for an alternative relation had already been pointed out by Hodge and co-workers [1], among others.

Gibson and Ashby [19] define the onset of densification as the boundary between plateau behavior and densification. The theoretical strain ε_D^{th} at which all pore space gets squeezed out should be [19]:

$$\varepsilon_D^{th} = 1 - \frac{\rho_f}{\rho_b} \tag{1}$$

where the ρ_f and ρ_b account for the Au foam and bulk Au density, respectively. However, based on experimental data, Gibson and Ashby define the densification strain ε_D, the strain for which all the empty space is crushed out, as

$$\varepsilon_D = 1 - 1.4 \cdot \left(\frac{\rho_f}{\rho_b} \right) \tag{2}$$

Our simulations show that the onset of densification occurs just after a strain of 0.3, when the instantaneous relative density goes beyond 0.6. Equation (1) predicts a theoretical densification strain of 0.75 whereas Eq. (2) predicts a densification strain of 0.65. Visualization of the MD structure reveals that at a strain of 0.6,
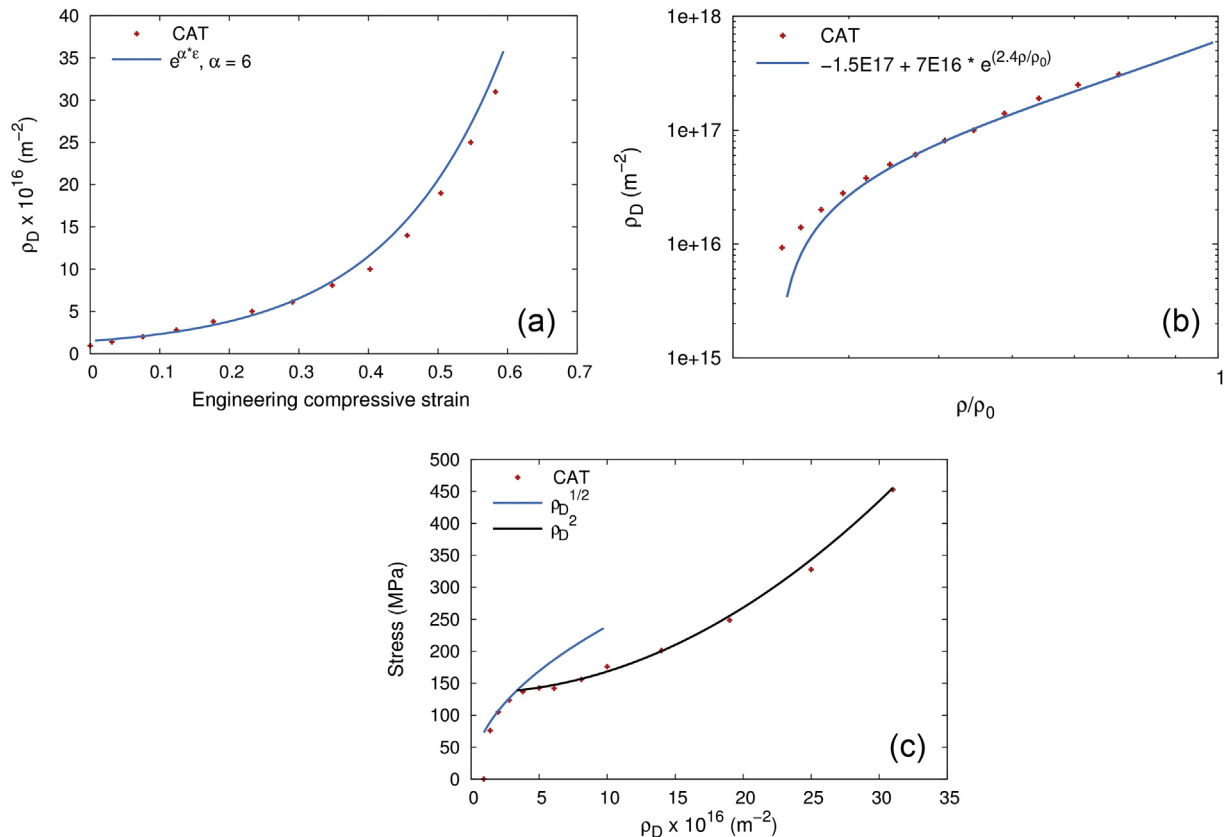

Fig. 3. Stress versus foam density plot, including our simulations, simple power law models, and the logarithmic model proposed in this paper.

Fig. 4. Dislocation density plots. (a) Dislocation density evolution with strain reveals an accumulation that follows an exponential law. (b) Dislocation density evolves following an exponential law as the foam densifies. (c) Once the plateau in the stress strain curve is reached, stress increases quadratically with dislocation density.

many voids are still present.

In our simulations, after the onset of densification, the process is characterized by a complex deformation pattern. The stress required for the densification rises rapidly as the open spaces between the collapsed cell structures close up.

Meyers and Chawla [35] propose treating the late densification of a powder by using the Carroll and Holt model [36], which was developed to describe the collapse of individual pores (voids) under hydrostatic pressure. Interestingly, the porosity as a function of time plots presented by Carroll and Holt [36] have the same pattern as the porosity evolution plot of Fig. 1. This fact suggests that an equation akin to the Carroll–Holt model could match the trends presented in our simulations for the densification regime.

Carroll and Holt presented the following equation relating hydrostatic pressure P on the collapsing void with the material yield stress σ_0 and the relative density D:

$$P = \frac{2}{3}\sigma_0 \ln\left(\frac{1}{1-D}\right) \qquad (3)$$

We employed a similar equation to the stress–strain curve in our simulations, using:

$$\sigma = \frac{2}{3}\sigma_{PP} \ln\left(\frac{1}{\varepsilon_D - \varepsilon}\right) \qquad (4)$$

which can also be presented as,

$$\sigma = \frac{2}{3}\sigma_{PP} \ln\left(\frac{1}{\varepsilon_D^{th} - \frac{\rho_f}{\rho_b}}\right) \qquad (5)$$

where σ_{PP} is the stress corresponding to the plastic plateau of the stress–strain plot. It must be noted that both ρ_f/ρ_b and ε in Eq. (4) and Eq. (5) must be taken as instantaneous values. The presentation of Eqs. (4) and (5) in Figs. 2 and 3 shows excellent agreement with our MD results.

Fig. 4 presents the results of the computed dislocation densities as function of (a) the applied strain, (b) the relative density, and (c) the stress. Fig. 5 presents four views of a 2 nm thick slice of the foam at different stages of deformation. Typical defect structures are shown. The majority of defects correspond to Shockley partials and stacking faults, in line with previous studies [2,22,37]. The dislocation density starts with a non-zero value due to the effect of the surface stress during relaxation, which even at zero strain introduces few defects into the foam, as shown in Fig. 5 a, these are Shockley partials and stacking faults, in agreement with Ngô et al.
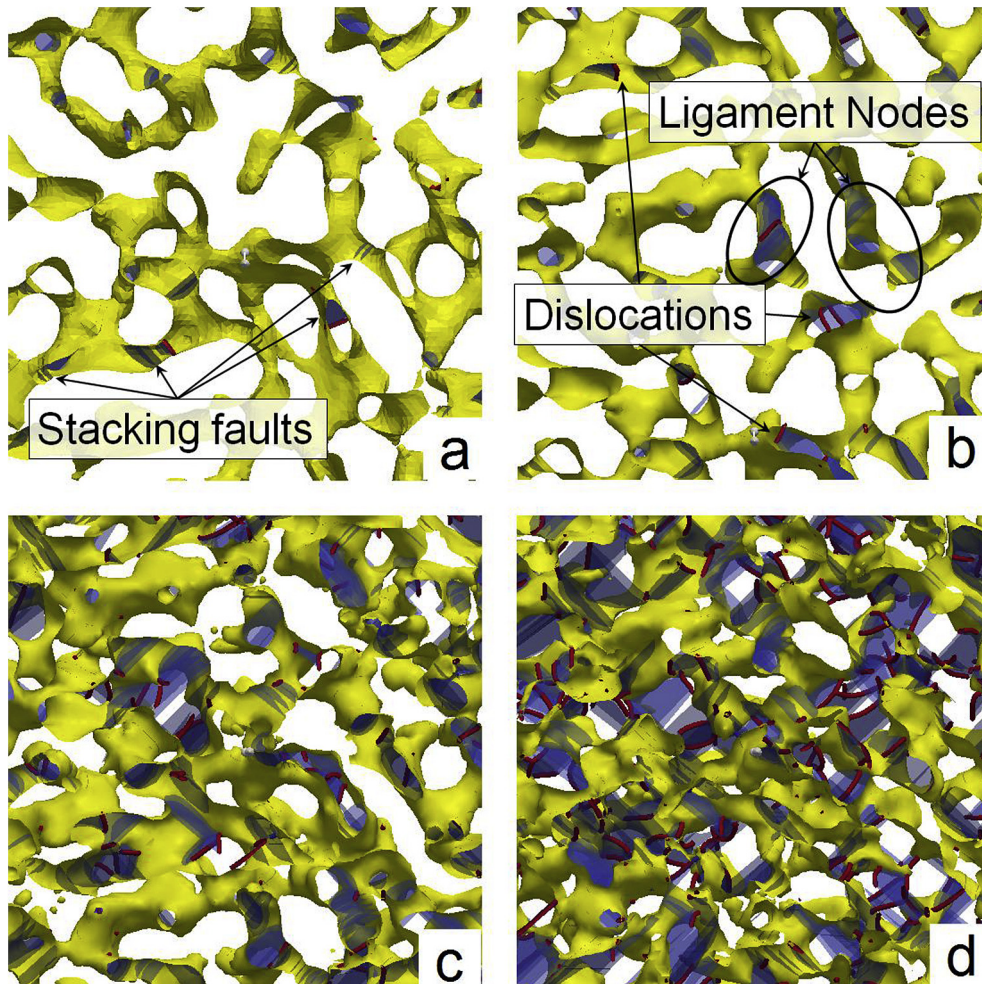

Fig. 5. Evolution of defects with strain for a 2 nm thick slice. (a). $\varepsilon = 0$; Linear (dislocations) and planar (stacking fault) defects can be observed in the relaxed structure, prior to deformation. (b) $\varepsilon = 0.14$; The amount of defects increases at ligament nodes. (c) $\varepsilon = 0.42$; Plasticity is now massive as porosity starts decreasing significantly. (d) $\varepsilon = 0.57$; Porosity is now half of the initial porosity. Ligaments are vastly populated by dislocations and stacking faults. Plasticity is now massive as porosity starts decreasing significantly.
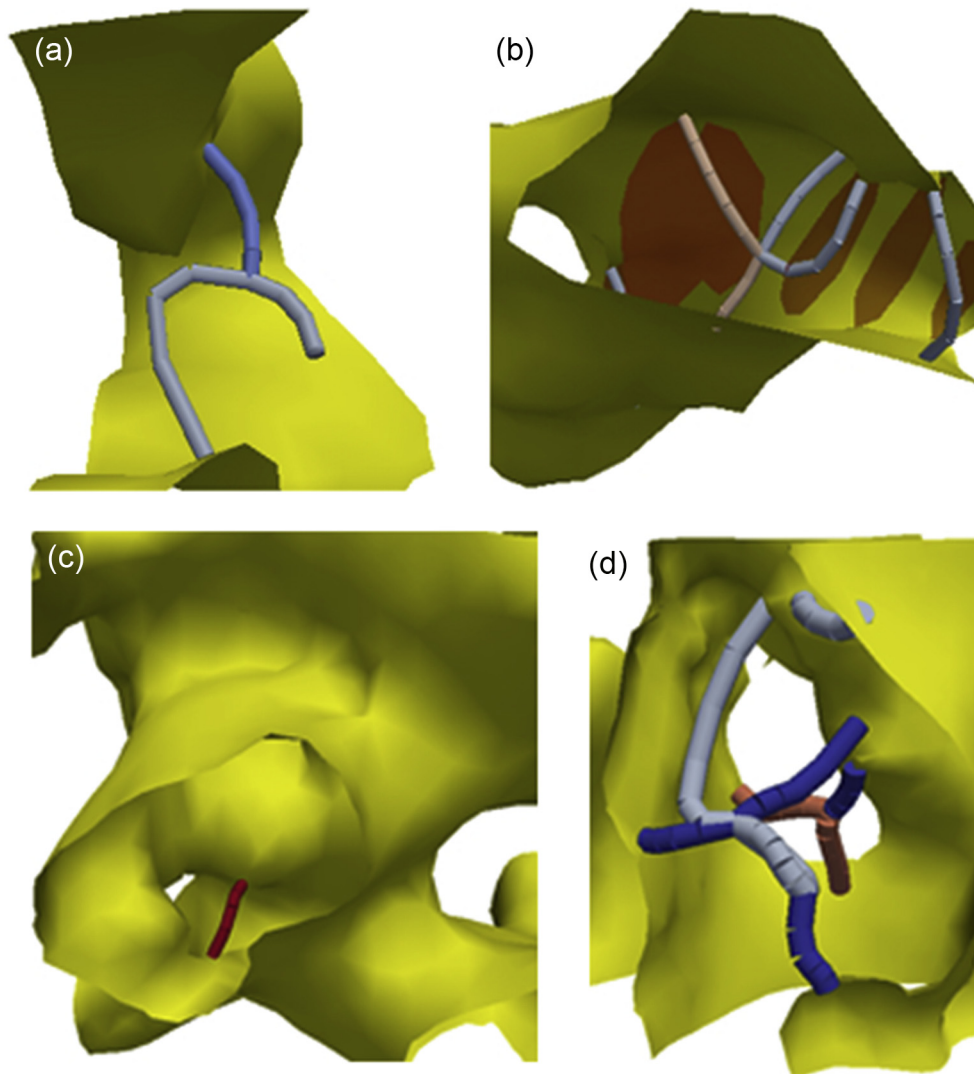
Fig. 6. Different defective structures present at 0.4 strain. Planar defects were intentionally removed from Figures a,c and d, for a clearer presentation of the dislocations. Inset (a) presents two Shockley partials (light-blue) reacting into a Lomer–Cottrel lock (blue). Inset (b) depicts the junction of Shockley partials (light-blue) with perfect dislocations (pink). The filament is also populated by stacking faults (light-brown). Inset (c) shows an isolated Frank partial dislocation (red). Inset (d) shows two complex junctions. At the front, Shockley partials (light-blue) pinned by sessile dislocations (blue). In the background, two Hirth partials (light-brown) form a junction with a double stair-rod sessile dislocation. Foam surfaces are depicted in yellow. (For interpretation of the references to colour in this figure legend, the reader is referred to the web version of this article.)

[37]. Dislocation density increases exponentially with strain from the very beginning of plasticity, by the continuous nucleation and propagation of dislocations producing a significant amount of stacking faults, again in agreement with the evolution of dislocation density with strain for the simulations by Ngô et al. [37]. By the end of the simulation, the dislocation density reached $3 \times 10^{17}\,\mathrm{m}^{-2}$. As a first approximation, we can consider that each ligament reaches that density and supposing a representative volume equal to the ligament size cube, then we can infer a population of 3–5 dislocations per ligament, which is indeed seen in the simulation snapshots, see Fig. 5 d, corresponding to the highest dislocation density calculation.

In terms of the relative density of the foam, the dislocation density increases roughly following an exponential relation (Fig. 4b). The fitting presented in Fig. 4 b predicts a dislocation density of $6 \times 10^{17}\,\mathrm{m}^{-2}$ at full densification. This high value suggests that further investigation is needed in quest for a scaling law matching the dislocation density evolution and providing a reasonable dislocation density at full densification. Of interest for

applications in constitutive modeling, the stress behavior with respect to the computed dislocation density can be divided into two stages, see Fig. 4 c. The first stage in which the dislocation density increases with a power law of 0.5 up to the plateau, and a second stage above a stress of 135 MPa (strain around 0.15, initiation of the stress plateau), where the stress as a function of dislocation density evolves following a quadratic law, valid even at stresses belonging to the densification regime.

3.2. Deformation mechanisms

Dislocation activity was identified inside the ligaments and analysis revealed the presence of stacking faults as a result of the nucleation and propagation of Shockley partials that originate at the ligament surface and evolve into it until they reach another surface, leaving stacking faults as a residue. The recent contributions of Sun et al. [22] and Ngô et al. [37] provided valuable insights into the deformation mechanisms of nanoporous gold. Sun et al. [22] focused their study on the deformation mechanisms under

tension, while Ngô et al. [37] concentrated on the deformation mechanisms under compression. Both studies identified Shockley partials and Lomer−Cottrel locks [38] as the main defects involved in the plastic deformation of the nanoporous gold. Analysis of our data by means of the Crystal Analysis tool confirm the results presented by Zepeda-Ruiz and co-workers for a gold nanofoam [39]. Fig. 6 presents details of the defective structure at 0.4 strain.

Fig. 6 a shows a junction of Shockley partials into a Lomer−Cottrel dislocation lock found in the deformed structure. Initially proposed by Lomer, this sessile dislocation can form by the reaction of two perfect dislocations $1/2a[\bar{1}10] + 1/2a[101] = 1/2a[011]$. The same reasoning was applied by Cottrel to Shockley partials $1/6a[\bar{1}\bar{2}1] + 1/6a[21\bar{1}] = 1/6a[1\bar{1}0]$. This sessile dislocation, also known as a stair-rod dislocation, contribute to strain hardening by impeding slip in (111) or $(11\bar{1})$ plane, acting as a barrier for any additional dislocation moving in these planes. Lomer−Cottrel locks account for 5% of the total dislocation length at 0.4 strain, while Shockley partials account for more than 75% of the total dislocation length. The Crystal Analysis Tool [28] was used to filter and classify the dislocations. The algorithm presents the dislocations inside a crystal by means an arrangement of a discrete number of dislocation segments. Dislocation length was then determined by summing the contributions of each dislocation type segment.

Fig. 6 b shows the junction of two Shockley partials with a perfect dislocation. During the course of the simulation, the ratio of total perfect dislocation length to total Shockley partial length increased from 0.016 at 0.2 strain to 0.043 at 0.4 strain, that is almost a three times increase. A similar trend has been reported by Ngô et al. [37].

Fig. 6 c depicts the presence of a Frank partial dislocation ($\vec{b} = 1/3a[111]$). This is another type of sessile dislocation in fcc metals. Their presence is our simulations is rare and accounts for less than one percent of the total dislocation length.

Fig. 6 d presents two junctions. In the background, a triple junction can be seen as two Hirth partials ($\vec{b} = 1/3a[001]$ and $\vec{b} = 1/3a[0\bar{1}0]$) are connected to a double stair-rod dislocation with $\vec{b} = 1/6a[022]$. A double stair-rod dislocation can be produced by the reaction of two Shockley partials $1/6a[\bar{2}11] + 1/6a[211] = 1/6a[022]$. The occurrence of this reaction has also been reported by Zepeda-Ruiz and co-workers in their study of deformation mechanisms of irradiated metallic nanofoams [39]. In front of the aforementioned triple junction, a four dislocation junction can be seen, with two Shockley partials pinned by sessile dislocations, depicted in blue. Interestingly, even though the filaments are less than 2 nm diameter in average, junctions and thick ligaments allowed for the nucleation of various types of dislocations.

Twinning was also identified in the current study, but the planar fault density is less than that of stacking faults vastly populating filaments. These findings also agree with the results presented by Ngô et al. [37].

4. Conclusions

In summary, we present an atomistic simulation study of the mechanical response of nanoporous Au under uniaxial compression focusing on hardening and deformation mechanisms taking place. The observations of plasticity are consistent with experimental studies of nanoporous gold using in situ nanoindentation in a TEM [40]. The main conclusions are:

- A densification regime was identified, with hardening that follows a logarithmic evolution proportional to the inverse of strain and a simple scaling law is presented to predict this behavior.
- Once the plastic plateau is reached, hardening evolves with stress following a quadratic power law with respect to dislocation density, indicating that nanofoams should not be treated considering Taylor hardening as an applicable model.
- Hirth and Frank partials were identified, starting from filament walls and filament junctions, contributing to hardening. The large fraction of partials also leads to twinning, as expected. Lomer−Cottrel dislocation locks were also observed, and they would also contribute to hardening. In addition to the partial dislocations found in previous work [35], perfect dislocations were also identified, despite filaments having a diameter below 5 nm. Larger filaments might include a larger fraction of full dislocations.

Nanofoams have unique mechanical properties at large strains. These simulations help quantify their behavior exploring valuable scaling laws which facilitate links to continuum models [41] and experiments.

Acknowledgments

Appendix A. Supplementary data

Supplementary data related to this article can be found at http://dx.doi.org/10.1016/j.actamat.2016.02.030.

References

[1] A. Hodge, J. Biener, J. Hayes, P. Bythrow, C. Volkert, A. Hamza, Scaling equation for yield strength of nanoporous open-cell foams, Acta Mater. 55 (4) (2007) 1343–1349.
[2] D. Farkas, A. Caro, E. Bringa, D. Crowson, Mechanical response of nanoporous gold, Acta Mater. 61 (9) (2013) 3249–3256.
[3] N.J. Briot, T.J. Balk, Developing scaling relations for the yield strength of nanoporous gold, Philos. Mag. (2015) 1–19.
[4] Y. Ding, M. Chen, J. Erlebacher, Metallic mesoporous nanocomposites for electrocatalysis, J. Am. Chem. Soc. 126 (22) (2004) 6876–6877.
[5] J. Snyder, T. Fujita, M. Chen, J. Erlebacher, Oxygen reduction in nanoporous metal-ionic liquid composite electrocatalysts, Nat. Mater. 9 (11) (2010) 904–907.
[6] A. Wittstock, V. Zielasek, J. Biener, C. Friend, M. Bäumer, Nanoporous gold catalysts for selective gas-phase oxidative coupling of methanol at low temperature, Science 327 (5963) (2010) 319–322.
[7] J. Erlebacher, M.J. Aziz, A. Karma, N. Dimitrov, K. Sieradzki, Evolution of nanoporosity in dealloying, Nature 410 (6827) (2001) 450–453.
[8] D. Kramer, R.N. Viswanath, J. Weißmüller, Surface-stress induced macroscopic bending of nanoporous gold cantilevers, Nano Lett. 4 (5) (2004) 793–796.
[9] J. Biener, A. Wittstock, L. Zepeda-Ruiz, M. Biener, V. Zielasek, D. Kramer, R. Viswanath, J. Weißmüller, M. Bäumer, A. Hamza, Surface-chemistry-driven actuation in nanoporous gold, Nat. Mater. 8 (1) (2009) 47–51.
[10] H.-J. Jin, X.-L. Wang, S. Parida, K. Wang, M. Seo, J. Weißmüller, Nanoporous Au−Pt alloys as large strain electrochemical actuators, Nano Lett. 10 (1) (2009) 187–194.
[11] X. Lang, L. Chen, P. Guan, T. Fujita, M. Chen, Geometric effect on surface enhanced raman scattering of nanoporous gold: improving raman scattering by tailoring ligament and nanopore ratios, Appl. Phys. Lett. 94 (21) (2009) 213109.
[12] E. Detsi, Z. Chen, W. Vellinga, P. Onck, J. De Hosson, Reversible strain by physisorption in nanoporous gold, Appl. Phys. Lett. 99 (8) (2011) 083104.
[13] L. Chen, T. Fujita, M. Chen, Biofunctionalized nanoporous gold for electrochemical biosensors, Electrochim. Acta 67 (2012) 1–5.
[14] L. Gibson, Mechanical behavior of metallic foams, Annu. Rev. Mater. Sci. 30 (1) (2000) 191–227.
[15] J. Biener, A.M. Hodge, A.V. Hamza, Microscopic failure behavior of nanoporous gold, Appl. Phys. Lett. 87 (12) (2005) 121908.
[16] J. Biener, A.M. Hodge, A.V. Hamza, L.M. Hsiung, J.H. Satcher Jr., Nanoporous Au: a high yield strength material, J. Appl. Phys. 97 (2) (2005) 024301.
[17] J. Biener, A.M. Hodge, J.R. Hayes, C.A. Volkert, L.A. Zepeda-Ruiz, A.V. Hamza,

F.F. Abraham, Size effects on the mechanical behavior of nanoporous Au, Nano Lett. 6 (10) (2006) 2379–2382.

[18] A. Mathur, J. Erlebacher, Size dependence of effective young's modulus of nanoporous gold, Appl. Phys. Lett. 90 (6) (2007) 1910.

[19] L.J. Gibson, M.F. Ashby, Cellular Solids: Structure and Properties, Cambridge University Press, 1997.

[20] X.-Q. Feng, R. Xia, X. Li, B. Li, Surface effects on the elastic modulus of nanoporous materials, Appl. Phys. Lett. 94 (1) (2009) 011916.

[21] R. Xia, C. Xu, W. Wu, X. Li, X.-Q. Feng, Y. Ding, Microtensile tests of mechanical properties of nanoporous Au thin films, J. Mater. Sci. 44 (17) (2009) 4728–4733.

[22] X.-Y. Sun, G.-K. Xu, X. Li, X.-Q. Feng, H. Gao, Mechanical properties and scaling laws of nanoporous gold, J. Appl. Phys. 113 (2) (2013) 023505.

[23] M. Kolluri, S. Karthikeyan, U. Ramamurty, Effect of lateral constraint on the mechanical properties of a closed-cell Al foam: I. Experiments, Metall. Mater. Trans. A 38 (2007) 2006–2013.

[24] S. Plimpton, Fast parallel algorithms for short-range molecular dynamics, J. Comp. Phys. 117 (1) (1995) 1–19.

[25] R. Johnson, Phase stability of fcc alloys with the embedded-atom method, Phys. Rev. B 41 (14) (1990) 9717.

[26] D.A. Crowson, D. Farkas, S.G. Corcoran, Geometric relaxation of nanoporous metals: the role of surface relaxation, Scr. Mater. 56 (11) (2007) 919–922.

[27] D.A. Crowson, D. Farkas, S.G. Corcoran, Mechanical stability of nanoporous metals with small ligament sizes, Scr. Mater. 61 (5) (2009) 497–499.

[28] A. Stukowski, V.V. Bulatov, A. Arsenlis, Automated identification and indexing of dislocations in crystal interfaces, Model. Simul. Mater. Sci. Eng 20 (8) (2012) 085007.

[29] A. Stukowski, Visualization and analysis of atomistic simulation data with OVITO – the open visualization tool, Model. Simul. Mater. Sci. Eng. 18 (1) (2010) 015012.

[30] A. Henderson, J. Ahrens, C. Law, et al., The ParaView Guide, Kitware, Clifton Park, NY, 2004.

[31] A. Stukowski, Computational analysis methods in atomistic modeling of crystals, JOM 66 (2014) 399–407.

[32] R. Dou, B. Derby, Deformation mechanisms in gold nanowires and nanoporous gold, Philos. Mag. 91 (7–9) (2011) 1070–1083.

[33] H.-J. Jin, L. Kurmanaeva, J. Schmauch, H. Rösner, Y. Ivanisenko, J. Weißmüller, Deforming nanoporous metal: role of lattice coherency, Acta Mater. 57 (9) (2009) 2665–2672.

[34] A.M. Hodge, J.R. Hayes, J.A. Caro, J. Biener, A.V. Hamza, Characterization and mechanical behavior of nanoporous gold, Adv. Eng. Mater. 8 (9) (2006) 853.

[35] M.A. Meyers, K.K. Chawla, Mechanical Behavior of Materials, vol. 2, Cambridge University Press Cambridge, 2009.

[36] M. Carroll, A. Holt, Static and dynamic pore-collapse relations for ductile porous materials, J. Appl. Phys. 43 (4) (1972) 1626–1636.

[37] B.-N.D. Ngô, A. Stukowski, N. Mameka, J. Markmann, K. Albe, J. Weißmüller, Anomalous compliance and early yielding of nanoporous gold, Acta Mater. 93 (2015) 144–155.

[38] D. Hull, D.J. Bacon, Introduction to Dislocations, vol. 257, Pergamon Press Oxford, 1984.

[39] L. Zepeda-Ruiz, E. Martinez, M. Caro, E. Fu, A. Caro, Deformation mechanisms of irradiated metallic nanofoams, Appl. Phys. Lett. 103 (3) (2013) 031909.

[40] Y. Sun, J. Ye, A.M. Minor, T.J. Balk, In situ indentation of nanoporous gold thin films in the transmission electron microscope, Microsc. Res. Tech. 72 (3) (2009) 232–241.

[41] N. Huber, R. Viswanath, N. Mameka, J. Markmann, J. Weißmüller, Scaling laws of nanoporous metals under uniaxial compression, Acta Mater. 67 (2014) 252–265.